High energy storage density and large strain in Bi(Zn2/3Nb1/3)O3-Doped BiFeO3-BaTiO3 ceramics

WANG, Dawei, FAN, Zhongming, LI, Wenbo, ZHOU, Di, FETEIRA, Antonio <http://orcid.org/0000-0001-8151-7009>, WANG, Ge, MURAKAMI, Shunsuke, SUN, Shikuan, ZHAO, Quanliang, TAN, Xiaoli and REANEY, Ian

ACS APPLIED ENERGY MATERIALS

Article

High Energy Storage Density and Large Strain in Bi(Zn2/3Nb1/3)O3-Doped BiFeO3-BaTiO3 Ceramics

Dawei Wang, Zhongming Fan, Wenbo Li, Di Zhou, Antonio Feteira, Ge Wang, Shunsuke Murakami, Shikuan Sun, Quanliang Zhao, Xiaoli Tan, and Ian M. Reaney

ACS Appl. Energy Mater., **Just Accepted Manuscript** • DOI: 10.1021/acsaem.8b01099 • Publication Date (Web): 16 Jul 2018

ACS Publications

is published by the American Chemical Society. 1155 Sixteenth Street N.W., Washington, DC 20036

High Energy Storage Density and Large Strain in $Bi(Zn_{2/3}Nb_{1/3})O_3$-Doped $BiFeO_3$-$BaTiO_3$ Ceramics

Dawei Wang[a]*, Zhongming Fan[b], Wenbo Li[c], Di Zhou[a,c], Antonio Feteira[d], Ge Wang[a], Shunsuke Murakami[a], Shikuan Sun[a], Quanliang Zhao[e], Xiaoli Tan[b], Ian M Reaney[a]*

[a]*Department of Materials Science and Engineering, University of Sheffield, Sheffield S1 3JD, UK*

[b]*Department of Materials Science and Engineering, Iowa State University, Ames, Iowa, 50011, USA*

[c]*Electronic Materials Research Laboratory, Key Laboratory of the Ministry of Education & International Center for Dielectric Research, Xi'an Jiaotong University, Xi'an 710049, Shaanxi, China*

[d]*Christian Doppler Laboratory for Advanced Ferroic Oxides, Sheffield Hallam University, Sheffield S1 1WB, UK*

[e]*School of Mechanical and Materials Engineering, North China University of Technology, Beijing 100144, China*

* Corresponding author. E-mail address: dawei.wang@sheffield.ac.uk, i.m.reaney@sheffield.ac.uk

ABSTRACT

High recoverable energy density (W_{rec} ~ 2.1 J/cm^3) was obtained in (0.7-x)$BiFeO_3$-0.3$BaTiO_3$-x$Bi(Zn_{2/3}Nb_{1/3})O_3$ + 0.1wt% Mn_2O_3 (BF-BT-xBZN, x = 0.05) lead-free ceramics at < 200 kV/cm. Fast discharge speeds (< 0.5 μs), low leakage (~ 10^{-7} A/cm^2) and small temperature variation in W_{rec} (~ 25% from 23 to 150 °C) confirmed the potential for these $BiFeO_3$ based compositions for use in high energy density capacitors. A core-shell microstructure composed of a $BiFeO_3$-rich core and $BaTiO_3$-rich shell was observed by scanning and transmission electron microscopy which may contribute to the high value of energy density. In addition, for x = 0.005, a large electromechanical strain was observed with S_{pos} = 0.463% and effective d_{33}^* ~ 424 pm/V, suggesting that this family of ceramics may also have potential for high strain actuators.

Keywords: energy storage, bismuth ferrite, lead-free ceramics, piezoelectrics, dielectrics, capacitors

INTRODUCTION

The current research into new energy storage materials is mainly driven by concerns regarding the continued use of fossil fuels for automotive applications. Therefore, low cost, sustainable and environmentally-friendly energy storage materials with high energy densities are required.[1-3] Among current energy storage devices, ceramic capacitors are emerging as promising technological alternatives to fuel cells and batteries, because of their high power densities combined with fast charge-discharges rates, which are favoured in advanced pulse power applications.[4-7] This drives the search for dielectrics exhibiting both high energy and power densities, to satisfy for power supply components incorporated into portable electronics, electric vehicles and other high power and energy storage applications.[8-10]

To attain high recoverable energy density (W_{rec}) and efficiency (η), a polarization maximum (P_{max}), a small remnance (P_r) and an optimised breakdown strength (BDS) are simultaneously required. Furthermore, the stability of devices in a range of temperature is also a critical parameter. For example, for hybrid electric vehicles these devices are expected to operate at temperatures ranging from -40 °C to 140 °C. [1,11] Consequently, ferroelectrics (FE) and antiferroelectrics (AFE) are promising candidates due to their high P_{max} and Curie temperature (T_C). The total energy density (W), W_{rec} and η of FE and AFE ceramics is given by:

$$W = \int_0^{P_{max}} E dP, \quad (1)$$

$$W_{rec} = \int_{P_r}^{P_{max}} E dP, \quad (2)$$

$$\eta = W_{rec}/W \quad (3)$$

where P, P_{max} and P_r are the polarization, polarization maximum and remnance, respectively.

Although there are commercial energy storage devices based on La doped lead zirconate titanate, concerns over the toxicity of PbO have led to a large body of recent research on lead free replacements such as $BaTiO_3$ (BT), $(K_{0.5}Na_{0.5})NbO_3$ (KNN) and $(Bi_{0.5}Na_{0.5})TiO_3$ (BNT) based

ceramics.[12-25] Oxide additives such as Al_2O_3, SiO_2, MgO enhance both W_{rec} and BDS in BT-based ceramics[12-14] but BT-$Bi(M,N)O_3$ (M = Li, Mg, Zn, N = Nb, Ti, Zr) ceramics show greater promise, with W_{rec} up to 2.5 J/cm^3.[15-21] In addition, $Bi_{0.5}Na_{0.5}TiO_3$-$BaTiO_3$-$KNbO_3$ (BNT-BT-KN) and $Bi_{0.5}Na_{0.5}TiO_3$-$BaTiO_3$-$NaTaO_3$ (BNT-BT-NT) also exhibit large W_{rec} of 1.72 and 1.2 J/cm^3, respectively.[22,23] In a recent study, Du et al. showed a commensurate improvement in W_{rec} to ~ 4 J/cm^3 in KNN-ceramics due to an enhancement of BDS (300~400 kV/cm), which was achieved by a careful control of grain growth.[24,25] $BiFeO_3$-$BaTiO_3$ (BF-BT) ceramics are characterised by high values of Curie maximum (T_C) and P_{max} (> 40 μC/cm^2) [26-32], but because their dielectric $tan\delta$ and P_r are relatively large, their energy storage characteristics have been seldom studied. Recently, Nb_2O_5, $La(Mg_{1/2}Ti_{1/2})O_3$, $Ba(Mg_{1/3}Nb_{2/3})O_3$ and Nd_2O_3 have been used as either dopants in, or in solid solution with, BF-BT with W_{rec} of 0.71, 1.66, 1.56, and 1.82 J/cm^3, respectively, reported[33-36] Nd doped BF-BT multilayers showed particular promise with both high W_{rec} ~ 6.74 J/cm^3 and η ~ 77%, from RT to 125 °C.[36]

Wu et al. theoretically predicted that FE ceramics with core-shell microstructure could achieve enhanced energy density and reduced energy loss.[37] However, to our knowledge, up to now the energy storage characteristics of BF-based ceramics featuring a core-shell microstructure remain elusive, as no experimental evidence has been provided. Also $Bi(Zn_{2/3}Nb_{1/3})O_3$ (BZN) doped BF-BT materials were recently reported to have excellent piezoelectric properties[27] but their energy storage performance is yet to be determined, despite each effect relying on a large remanent/induced polarisation. In this work, a unique core-shell microstructure was induced by the substitution of BZN into BF-BT, its impact on the structure-property relationships, in particular on the energy storage characteristics, evaluated.

EXPERIMENTAL SECTION

Ceramic synthesis and characterisation: $(0.7\text{-}x)BiFeO_3$-$0.3BaTiO_3$-$xBi(Zn_{2/3}Nb_{1/3})O_3$ + 0.1wt% Mn_2O_3 (BF-BT-xBZN, x = 0, 0.005, 0.01, 0.02, 0.05, 0.08) ceramics were fabricated using solid state reaction.[26,36] In order to increase the resistivity of ceramics, 0.1 wt% Mn_2O_3 was added into the

calcined powder of BF-BT-xBZN.[26,28,36] Mn-ions are considered to form defect dipoles with oxygen vacancies and decrease their mobility. Densities of ceramics were determined by the Archimedes immersion method and were typically >95%. The phase structure of sintered ceramics was determined at RT by X-ray powder diffraction (XRD) using a Bruker D2 Phaser. Grain and sub-grain structures were evaluated by scanning electron microscope (SEM) and transmission electron microscopy (TEM) using an FEI Inspect F50 equipped with a backscattered (BSE) detector and a Tecnai G2-F20, respectively. For SEM, ceramics were ground/polished to a mirror finish using wet abrasive paper and diamond paste (MetPrep Ltd.). For TEM, BF-BT-0.05BZN ceramics were ground to 120 μm, 3 mm disks ultrasonically cut and their centers dimpled down to 10 μm. Prior to Ar-ion milling to achieve electron transparency, samples were annealed at 650 °C/0.5 h to ensure that residual stresses were removed.

Electrical properties: Fired-on gold paste electrodes were applied to both surfaces of the ceramics. 100-120 °C was used to pole the electroded ceramics at fields of 40 ~ 60 kV/cm. A ferroelectric tester (aixACCT TF 2000E) was employed to measure the polarization and the electric-field induced strain from -50 °C to 150 °C using a 1 Hz triangular signal at provided by a TREK power supply. Leakage current density was also measured using the aixACCT TF 2000E. The dielectric properties as a function of temperature were evaluated from RT to 650 °C using an LCR meter (Agilent 4184A). AC impedance spectroscopy was carried out at 400 °C using a second LCR Meter (Agilent E4980A). Charging-discharge characteristics were determined using a capacitor discharge circuit.[16,36] A Tektronix DPO 4104 oscilloscope together with a Pearson 6585 coil were employed to obtain the discharge current waveforms. The discharge energy was then measured using ceramics connected in series with a load resistor (RL).

RESULTS AND DISCUSSION

Room temperature XRD data in the 20°~70° 2θ range for BF-BT-xBZN ceramics are illustrated in Fig. 1(a). Reflections are ascribed to either a single-phase perovskite or a mixture of perovskite phases, without any detectable secondary impurity phases for $x < 0.08$. Secondary peaks however,

were observed for x = 0.08, denoting the solid solubility limit for $Zn_{1/3}/Nb_{2/3}$ self-compensated doping in BF-BT. The average ionic radii, R, of $(Zn_{2/3}Nb_{1/3})^{3+}$ ions is given by R = 2/3R(Zn^{2+}) + 1/3R(Nb^{5+}) = 0.707 Å (0.74 Å and 0.64 Å are the respective ionic radii of Zn^{2+} and Nb^{5+}),[38] which is larger than that of Fe^{3+} and Ti^{4+} (0.645 Å and 0.605, respectively) and consistent with the diffraction peaks shifting to lower diffraction angle with increasing BZN concentration (Fig.1). The likely crystal symmetry is often determined by (021)/(110) peak splitting at ~2θ = 32°. In the present case, expanded XRD patterns reveal an apparent coexistence of rhombohedral (*R*) and pseudocubic (*PC*) symmetries at room temperature in BF-BT-xBZN ceramics, as corroborated by broad multiple peaks. To confirm the phase assemblage, Rietveld refinement of BF-BT-0.05BZN was carried out using a two-phase refinement method (*R3c* + $Pm\bar{3}m$) in the GSAS+EXPGUI package.[39,40] Observed and calculated patterns were in good agreement for BF-BT-0.05BZN as demonstrated in Fig. 1(b) (R_p = 7.6%, R_{wp} = 9.7% and chi-squared (χ^2) = 2.3), corroborating the presence of *PC* ($Pm\bar{3}m$) and *R* (*R3c*) symmetries.

The relative permittivity (ε_r) and dielectric loss (*tan* δ) for BF-BT-xBZN ceramics from RT to 550 °C measured at 100 kHz are illustrated in Fig. 1(c). BF-BT and BF-BT-0.005BZN exhibit a relatively sharp peak in ε_r at 476 °C and 480 °C, respectively, associated with a ferroelectric to paraelectric transition (T_C) on heating but with increasing BZN concentration, two broad dielectric maxima are observed, each at lower temperatures. Furthermore, compared with BF-BT and BF-BT-0.005BZN, the maximum dielectric permittivity (ε_m) of BF-BT-xBZN (x > 0.005) decreases significantly and is accompanied by the emergence of broad frequency-dependent dielectric peaks (Fig. 1c). These two modifications are a manifestation of polar coupling disruption brought in by replacement of $(Zn_{2/3}Nb_{1/3})^{3+}$ for Fe^{3+}. Despite these changes, *tan* δ remains < 0.15 at < 230 °C, and then increases greatly (Fig. 1c), presumably due to a rise in *dc* conductivity. To evaluate the electrical homogeneity, impedance spectroscopy (IS) analysis was performed at 400 °C, Fig. 1(d) and Fig. S1. Indeed, electrical homogeneity can be qualitatively assessed from Z'' and M'' spectroscopic plots constructed from IS data.[41,42] It is evident that the peak positions of Z" and M" are almost coincident for BF-BT (Fig. S1a of ESI), however a frequency offset between the Z" and M" peak is observed for BF-BT-

0.02BZN and BF-BT-0.05BZN (Fig. 1d and Fig. S1b of ESI). This shows the latter compositions to be electrically heterogeneous, which we interpret on balance of evidence as arising from compositional inhomogeneity.

The SEM images of as-sintered and polished surface for BF-BT-xBZN are illustrated in Fig. S2 and Fig. 2(a-c), respectively. All samples present a single modal grain size distribution around an average of ~4 μm (Fig. S2 of ESI). Except for BF-BT and BF-BT-0.005BZN ceramics, there is evidence of core shell microstructure for BF-BT-xBZN (Fig. 2a-c), with dark and light contrast relating to $BaTiO_3$-rich and $BiFeO_3$-rich regions according to energy dispersive X-ray spectroscopy (EDS) mapping (Fig. 2d-k). The EDS elemental maps of polished BF-BT-0.05BZN samples are shown in Fig. 2(d-k). The Ba and Ti signals are weaker in the brighter regions of the SEM image, associated with the grain cores (Fig. 2d and e). Conversely, Bi and Fe exhibit a slightly increased intensity in the brighter areas (Fig. 2f, g). These results indicate that the observed core-shell microstructure in BF-BT-xBZN are associated with the micro-segregation of Ba and Ti into the shell, while Bi and Fe are concentrated in the core regions.[41-47.] Murakami et al. investigated the role of composition and quenching on core-shell formation in $BiMg_{1/3}Nb_{2/3}O_3$ doped BF-BT ceramics.[41,42] They concluded that the major influence was the onset of immiscibility on cooling from the sintering temperature, driven by the electronegativity difference of the dopant species. Effectively, the more covalent the dopants, the greater the tendency for immiscibility.

To examine the core-shell microstructure, TEM was conducted on BF-BT-0.05BZN ceramics. For further data on undoped systems the reader is referred to ref. 36. Fig. 3a is bright-field (BF) TEM image of a grain close to a $<211>_{pc}$ zone axis. The dark spherical region in the grain center corresponds to the bright regions in the SEM images in Figure 2 and is thus $BiFeO_3$ rich. $<211>_{pc}$ zone axis diffraction patterns (Fig. 2a) from the $BiFeO_3$ rich core have {½½½} superstructure reflections arising from antiphase O-octahedral tilting consistent with an *R3c* phase.[36] These superstructure reflections are absent in the shell regions which are $BaTiO_3$-rich, suggesting that they are *PC*. The weak aligned contrast in the shell region is consistent with relaxor-like phases in which

there is nano- rather than micro- or meso-range correlation of dipoles, commensurate with the diffuse frequency dependent Curie maxima, Fig. 3(b). The core and shell structures shown in Fig 3(a) and in Fig. 2 have been tentatively assigned to the high ($BiFeO_3$-rich) and low ($BaTiO_3$-rich) temperature broad Cure maxima in Fig. 3(b).

Field-induced polarization (*P*-*E*), bipolar strain (*S*-*E*) and unipolar strain curves for BF-BT-xBZN ceramics measured at 100 kV/cm are illustrated in Fig. 4(a-c) (no field-induced strain for BF-BT-0.08BZN was detected). P_r, coercive field (E_C) and electric-field induced positive (S_{pos}) and negative strain (S_{neg}) as a function of x are summarized in Fig. 4(d,e). The large signal piezoelectric strain coefficient (d_{33}^*) and hysteresis (*SH*) are calculated by

$$d_{33}^* = S_{max}/E_{max}, \quad (5)$$

$$SH = H_{Emax/2}/S_{max}, \quad (6)$$

where S_{max}, E_{max} and $H_{Emax/2}$ is the average electric field induced maximum strain obtained from the unipolar strain loops, the maximum electric field and the width of the loop at half the applied field, respectively.[48] BF-BT and BF-BT-0.005BZN ceramics exhibit saturated polarization loops and butterfly-shaped strain loops at 100 kV/cm (Fig. 4a,b), which also corroborate the high electrical resistivity of these ceramics. With increasing BZN content, the *P*-*E* and *S*-*E* loops become slimmer and are no longer saturated (Fig. 4a,b), along with P_r, E_C, d_{33} and S_{neg} continuously decreasing (Fig. 4d,e), suggestive of relaxor-like behavior, which is commensurate with both the broad ε_m (Fig. 1c) and nanodomain structure (Fig. 3). The largest $P_r \sim 24.6$ μC/cm^2, $E_C \sim 32.8$ kV/cm, $d_{33} \sim 180$ pC/N, $S_{neg} \sim 0.079\%$ values and smallest *HS* ~ 18.4% value are exhibited by BF-BT ceramics (Fig. 4d,e,f), due to coexistence of *R3c* and *PC* symmetries (Fig. 1).[26,36] On the other hand, the largest $S_{pos} \sim 0.463\%$ and $d_{33}^* \sim 424$ pm/V values are exhibited by BF-BT-0.005BZN ceramics (Fig. 4e,f), which arises from a field-induced transition from short- to long-range dipolar order at the transition from a normal to a relaxor ferroelectric (Fig. 4a,b and Fig. 1c).[26,36]

Because of their slim *P*-*E* loops (Fig. 4a), BF-BT-0.05BZN and BF-BT-0.08BZN exhibit a greater potential for energy storage and were selected for further characterization. Unipolar *P*-*E* loops are

illustrated in Fig. 5(a,b), with corresponding values of P_{max}, P_r and ΔP (P_{max} - P_r) at different electric fields given in Fig. S3. As the increase of electric field, P_{max} and ΔP are found to increase linearly with a marginal improvement of P_r for both samples (Fig. S3). The highest values of P_{max} and ΔP are 36.7 and 32.8 μC/cm^2 for BF-BT-0.05BZN at 180 kV/cm, 26.4 and 24.5 μC/cm^2 for BF-BT-0.08BZN at 190 kV/cm, respectively. Equations 1-3 are employed to calculate W, W_{rec} and η , Fig. 5(c,d). As field increases, W and W_{rec} increase, reaching 3.7 and 2.06 J/cm^3 for BF-BT-0.05BZN at 180 kV/cm, and 2.9 and 1.98 J/cm^3 cm^2 for BF-BT-0.08BZN at 190 kV/cm, respectively. The η values, however, decrease for both compositions to 53% for BF-BT-0.05BZN at 180 kV/cm and 68% for BF-BT-0.08BZN at 190 kV/cm.

The discharge behaviour, leakage current and temperature stability are critical for high power capacitors. The discharge behaviour of BF-BT-0.05BZN and BF-BT-0.08BZN as a function of applied field is given in Fig. 6. The current increases as the electric field increases from 40 kV/cm to 70 kV/cm and all discharge processes occur within ~0.5 μs, as shown in Fig. 6(a,b). The time for the discharge energy in the load to achieve 90% of the final value (τ_{90}), is obtained from the W_{rec} curves (Fig. 6c,d). $\tau_{0.9}$ of both composition under different electric fields is less than 0.1 μs.

In-situ temperature dependence of leakage current density (J) and unipolar *P-E* loops at 120 kV/cm for BF-BT-0.05BZN are shown in Fig. 7(a,b). The corresponding values of J, P_{max}, P_r and ΔP are given in Fig. 7(c) and Fig. S4. W, W_{rec} and η are also calculated and plotted in Fig. 7(d). The value of J below 50 °C is of the order of 10^{-7} A/cm^2 in the high field region (Fig. 7a,c), ~ one order magnitude less than reported for BF-based ceramics at RT.[49,50] From -50 °C to 150 °C, J consistently increases (Fig. 7a,c), indicating increased conductivity at high temperatures. As temperature increases, saturated *P-E* loops are obtained at ~150 °C, giving increased values of P_{max} and P_r (Fig. S4), which is attributed to lower activation energy of the transition from relaxor to ferroelectric.[26,36] W increases with temperature, while W_{rec} and η

increase before decreasing from a maximum of 1 J/cm^3 and 59% at 75-100 °C, Fig. 7(d). The variation in W_{rec} is ~ 25% between RT and 150 °C, which is attractive for commercial applications.

A comparison of W_{rec} and strain for ceramics is plotted in Fig. 8.[12-25, 26-36, 48-92] W_{rec} generally increases with electric field but lead-based ceramics still exhibit larger W_{rec} values compared to the lead-free ceramics (Fig. 8a). To our knowledge, BF-BT-0.05BZN has one of the highest value of W_{rec} ~ 2.1 J/cm^3 among current lead-free FE ceramics with an electric field < 220 kV/cm, which is ascribed to the high BDS ~ 190 kV/cm, P_{max} ~ 36.7 μC/cm^2 and ΔP ~ 32.8 μC/cm^2. In Fig. 8(b), BF-BT-0.005BZN has one of the highest values of strain ~ 0.463% amongst ferroelectric ceramics, with a medium value of d_{33}^* ~ 424 pm/V and a low value of strain hysteresis ~38% (in comparison with BNT),[82-89] which is attractive for actuator applications. Core-shell structures in FE ceramics are reported to alleviate inhomogeneity of local electric fields and weakens dielectric nonlinearity, resulting in slimmer hysteresis loops.[37] Although the work presented does not conclusively prove the arguments presented by the authors of ref. 37, enhanced energy storage is observed for core-shell BT-BF-xBZN compositions. Furthermore, we note that recent multilayering of Nd doped BF-BT ceramics improved W_{rec} from 1.82 to 6.74 J/cm^3 and η from 50 to 77%.[36] Similar improvements for multilayers of BF-BT-xBZN whose bulk ceramics have superior energy storage properties would suggest that they have potential for commercialization should lead based systems fail to gain exemption from future environmental legislation. Moreover, BT-BF-xBZN compositions are rare-earth (RE)-free, lowering their cost and enhancing their potential for sustainable manufacturing.

CONCLUSIONS

Dense BF-BT-xBZN lead-free ceramics were fabricated using solid state reaction. *R* and *PC* phases coexisted in all studied BF-BT-xBZN compositions at RT. As BZN concentration increased, a core-shell microstructure was observed with a $BaTiO_3$-rich shell and $BiFeO_3$-rich core, confirmed by SEM, EDS, IS, TEM and LCR measurements. With the increase of BZN concentration, relaxor-like behaviour dominated with P_r, E_C, d_{33} and S_{neg} decreasing. The highest values of P_r ~ 24.6 μC/cm^2, E_C ~

32.8 kV/cm, d_{33} ~ 180 pC/N, S_{neg} ~ 0.079% and HS ~ 18.4% were achieved for the undoped BF-BT. The highest value of S_{pos} ~ 0.463% and d_{33}^* ~ 424 pm/V was obtained for BF-BT-0.05BZN. For energy storage properties, with increasing electric field, W and W_{rec} increased from 3.7 and 2.06 J/cm^3 for BF-BT-0.05BZN at 180 kV/cm, and 2.9 and 1.98 J/cm^3 cm^2 for BF-BT-0.08BZN at 190 kV/cm, respectively. η decreased however, to 53% for BF-BT-0.05BZN at 180 kV/cm and 68% for BF-BT-0.08BZN at 190 kV/cm, respectively. A fast discharge speed (less than 0.5 ms), leakage current ~ 10^{-7} A/cm^2 and a small temperature variation in W_{rec} (~ 25% in a temperature range between RT and 150 °C) were also obtained, suggesting that the BF-BT-xBZN is a potential lead-free candidate for pulsed power capacitors and electromechanical actuators.

ASSOCIATED CONTENT

Supporting Information.

This material is available free of charge via the Internet at http://pubs.acs.org.

Spectroscopic plots of Z'' and M'' for (a) BF-BT and (b) BF-BT-0.02BZN. SEM images of BF-BT-xBZN (a) x = 0, (b) x = 0.005, (c) x = 0.01, (d) x = 0.02, (e) x = 0.05 and (f) x = 0.08. P_{max}, P_r and ΔP for (a) BF-BT-0.05BZN and (b) BF-BT-0.08BZN. Temperature dependence of P_{max}, P_r and ΔP for BF-BT-0.05BZN at 120 kV/cm. The schematic diagram of the discharge circuit.

AUTHOR INFORMATION

Corresponding Author

***E-mail:** dawei.wang@sheffield.ac.uk, i.m.reaney@sheffield.ac.uk

Notes

The authors declare no competing financial interest.

ACKNOWLEDGMENT

This work was supported by the Engineering and Physical Sciences Research Council (EP/L017563/1 and EP/N010493/1) and National Natural Science Foundation of China (51602060 and 51402005).

REFERENCES

1. Chu B., Zhou X., Ren K., Neese B., Lin M., Wang Q., Bauer F., Zhang Q. M., A dielectric polymer with high electric energy density and fast discharge speed, Science, 2006, 313, 334-336.
2. Li Q., Chen L., Gadinski M. R., Zhang S., Zhang G., Li H., Haque A., Chen L., Jackson T., Wang Q., Flexible high-temperature dielectric materials from polymer nanocomposites, Nature, 2015, 523, 576-579.
3. Zhao L., Liu Q., Gao J., Zhang S., Li J. F., Lead-free antiferroelectric silver niobate tantalate with high energy storage performance, Adv. Mater. 2017, 29, 1701824-7pp.
4. Love G. R., Energy-storage in ceramic dielectrics, J. Am. Ceram. Soc., 1990, 73, 323–328.
5. Kwon S., Hackenberger W., Alberta E., Furman E., Lanagan M., Nonlinear Dielectric Ceramics and Their Applications to Capacitors and Tunable Dielectrics, IEEE Electr. Insul. Mag., 2011, 27, 43–55.
6. Hu W. B., Liu Y., Withers R. L., Frankcombe T. J., Noren L., Snashall A., Kitchin M., Smith P., Gong B., Chen H., Schiemer J., Brink F., Leung J. W., Electron-pinned defect-dipoles for high-performance colossal permittivity materials, Nat. Mater., 2013, 12, 821–826.
7. Li Q., Zhang G., Liu F., Han K., Gadinski M. R., Xiong C., Wang Q., Solution-processed ferroelectric terpolymer nanocomposites with high breakdown strength and energy density utilizing boron nitride nanosheets, Energy Environ. Sci., 2015, 8, 922–931.
8. Liu C., Li F., Ma L. P., Cheng H. M., Advanced Materials for Energy Storage, Adv. Mater., 2010, 22, E28–E62.
9. Hadjipaschalis I., Poullikkas A., Efthimiou V., Overview of current and future energy storage technologies for electric power applications, Renew. Sust. Energy Rev., 2009, 13, 1513–1522.
10. Chen H., Cong T. N., Yang W., Tan C., Li Y., Ding Y., Progress in electrical energy storage system: A critical review, Prog. Nat. Sci., 2009, 19, 291–312.
11. Wang Y. L., Chen X. L., Zhou H. F., Fang L., Liu L. J., Zhang H., Evolution of phase transformation behavior and dielectric temperature stability of BaTiO3-Bi(Zn0.5Zr0.5)O-3 ceramics system, J. Alloys Compd., 2013, 551, 365–369.

12. Liu B. B., Wang X. H., Zhao Q. C., Li L. T., Improved Energy Storage Properties of Fine-Crystalline BaTiO3 Ceramics by Coating Powders with Al2O3 and SiO2, J. Am. Ceram. Soc., 2015, 98, 2641–2646.
13. Zhang Q. M., Wang L., Luo J., Tang Q., Du J., Ba0.4Sr0.6TiO3/MgO Composites with Enhanced Energy Storage Density and Low Dielectric Loss for Solid-State Pulse-Forming Line, Int. J. Appl. Ceram. Technol., 2010, 7, E124–E128.
14. Huang Y. H., Wu Y. J., Qiu W. J., Li J., Chen X. M., Enhanced energy storage density of Ba0.4Sr0.6TiO3-MgO composite prepared by spark plasma sintering, J. Eur. Ceram. Soc., 2015, 35, 1469–1476.
15. Li W. B., Zhou D., L. Pang X., Enhanced energy storage density by inducing defect dipoles in lead free relaxor ferroelectric BaTiO3-based ceramics, Appl. Phys. Lett., 2017, 110, 132902-5pp.
16. Li W. B., Zhou D., Pang L. X., Xu R., Guo H. H., Novel barium titanate based capacitors with high energy density and fast discharge performance, J. Mater. Chem. A, 2017, 5, 19607–19612.
17. Yuan Q., Yao F., Wang Y., Ma R., Wang H., Relaxor ferroelectric 0.9BaTiO(3)-0.1Bi(Zn0.5Zr0.5)O3 ceramic capacitors with high energy density and temperature stable energy storage properties, J. Mater. Chem. C, 2017, 5, 9552-9558.
18. Wang T., Jin L., Li C. C., Hu Q. Y., Wei X. Y., Relaxor Ferroelectric BaTiO3-Bi(Mg2/3Nb1/3)O3 Ceramics for Energy Storage Application, J. Am. Ceram. Soc., 2015, 98, 559–566.
19. Hu Q. Y., Jin L., Wang T., Li C. C., Xing Z., Wei X. Y., Dielectric and temperature stable energy storage properties of 0.88BaTiO3-0.12Bi(Mg1/2Ti1/2)O3 bulk ceramics, J. Alloys Compd., 2015, 640, 416–420.
20. Shen Z. B., Wang X. H., Luo B. C., Li L. T., BaTiO3-BiYbO3 perovskite materials for energy storage applications, J. Mater. Chem. A, 2015, 3, 18146–18153.
21. Wu L. W., Wang X. H., Li L. T., Lead-free BaTiO3-Bi(Zn2/3Nb1/3)O-3 weakly coupled relaxor ferroelectric materials for energy storage, RSC Adv., 2016, 6, 14273–14282.

22. Xu Q., Xie J., He Z. C., Zhang L., Cao M. H., Huang X. D., Lanagan M. T., Hao H., Yao Z. H., Liu H. X., Energy-storage properties of Bi0.5Na0.5TiO3-BaTiO3-KNbO3 ceramics fabricated by wet-chemical method, J. Eur. Ceram. Soc., 2017, 37, 99–106.

23. Xu Q., Liu H. X., Zhang L., Xie J., Hao H., Cao M. H., Yao Z. H., Lanagan M. T., Structure and electrical properties of lead-free Bi0.5Na0.5TiO3-based ceramics for energy-storage applications, RSC Adv., 2016, 6, 59280–59291.

24. Yang Z. T., Du H. L., Qu S. B., Hou Y. D., Ma H., Wang J. F., Wang J., Wei X. Y., Xu Z., Significantly enhanced recoverable energy storage density in potassium-sodium niobate-based lead free ceramics, J. Mater. Chem. A, 2016, 4, 13778–13785.

25. Shao T. Q., Du H. L., Ma H., Qu S. B., Wang J., Wang J. F., Wei X. Y., Xu Z., Potassium-sodium niobate based lead-free ceramics novel electrical energy storage materials, J. Mater. Chem. A, 2017, 5, 554–563.

26. Wang D., Khesro A., Murakami S., Feteira A., Zhao Q., Reaney I. M., Temperature dependent, large electromechanical strain in Nd-doped BiFeO3-BaTiO3 lead-free ceramics, J. Eur. Ceram. Soc., 2017, 37, 1857–1860.

27. Lee M. H., Kim D. J., Park J. S., Kim S. W., Song T. K., Kim M. H., Kim W. J., Do D., Jeong I. K., High-Performance Lead-Free Piezoceramics with High Curie Temperatures, Adv. Mater., 2015, 27, 6976–6982.

28. Leontsevw S. O., Eitel R. E., Dielectric and Piezoelectric Properties in Mn-Modified (1-x)BiFeO3–xBaTiO3 Ceramics, J. Am. Ceram. Soc., 2009, 92, 2957–2961.

29. Fan Q., Zhou C., Zeng W., Cao L., Yuan C., Rao G., Li X., Normal-to-relaxor ferroelectric phase transition and electrical properties in Nb-modified 0.72BiFeO3-0.28BaTiO3 ceramics, J. Electroceram., 2016, 36, 1–7.

30. Malik R. A., Hussain A., Song T. K., Kim W. J., Ahmed R., Sung Y. S., Kim M. H., Enhanced electromechanical properties of (1-x)BiFeO3–BaTiO3–xLiNbO3 ceramics by quenching process, Ceram. Inter., 2017, 43, S198–S203.

31. Kim S., Khanal G. P., Nam H. W., Fujii I., Ueno S., Moriyoshi C., Kuroiwa Y., Wada S., Structural and electrical characteristics of potential candidate lead-free BiFeO3-BaTiO3 piezoelectric ceramics, J. Appl. Phys., 2017, 122, 164105.
32. Liu Z., Zheng T., Zhao C., Wu J., Composition design and electrical properties in BiFeO3-BaTiO3-Bi(Zn0.5Ti0.5)O3 lead-free ceramics, J. Mater. Sci.: Mater. Electron., 2017, 28, 13076–13083.
33. Wang T., Jin L., Tian Y., Shu L. L., Hu Q. Y., Wei X. Y., Microstructure and ferroelectric properties of Nb2O5-modified BiFeO3-BaTiO3 lead-free ceramics for energy storage, Mater. Lett., 2014, 137, 79–81.
34. Zheng D. G., Zuo R. Z., Zhang D. S., Li Y., Novel BiFeO3-BaTiO3-Ba(Mg1/3Nb2/3)O3 Lead-Free Relaxor Ferroelectric Ceramics for Energy-Storage Capacitors, J. Am. Ceram. Soc., 2015, 98, 2692–2695.
35. Zheng D. G., Zuo R. Z., Enhanced energy storage properties in La(Mg1/2Ti1/2)O3-modified BiFeO3-BaTiO3 lead-free relaxor ferroelectric ceramics within a wide temperature range, J. Eur. Ceram. Soc., 2017, 37, 413–418.
36. Wang D., Fan Z., Zhou D., Khesro A., Murakami S., Feteira A., Zhao Q., Tan X., Reaney I. M, Bismuth ferrite-based lead free ceramics and multilayers with high recoverable energy density, J. Mater. Chem. A, 2018, 6: 4133–4144.
37. Wu L., Wang X., Li L., Enhanced Energy Density in Core–Shell Ferroelectric Ceramics: Modeling and Practical Conclusions, J. Am. Ceram. Soc., 2016, 99, 930–937.
38. Shannon R. D., Revised effective ionic radii and systematic studies of interatomic distances in halides and chalcogenides, Acta Cryst., 1976, A32, 751–767.
39. Larson C., Von Dreele R. B., General Structure Analysis System (GSAS), Los Alamos: Los Alamos National Laboratory Report LAUR; 2004.
40. Toby H., a graphical user interface for GSAS, J. Appl. Cryst., 2001, 34, 210–213.
41. Murakami S., Ahmed N. T. A. F., Wang D., Feteira A., Sinclair D. C., Reaney I. M, Optimising properties in BiMeO3 (Me = Al, Ga, Sc, Y, Mg2/3Nb1/3, Zn2/3Nb1/3, Zn1/2Ti1/2) doped lead-

free BaTiO3-BiFeO3 based ceramics for actuator applications, J. Eur. Ceram. Soc., 2018, 38, 4220-4231.

42. Murakami S., Wang D., Mostaed A., Khesr A., Feteira A., Sinclair D. C., Reaney I. M, High strain (0.4%) Bi(Mg2/3Nb1/3)O3-BaTiO3-BiFeO3 lead-free piezoelectric ceramics and multilayers, J. Am. Ceram. Soc., 2018, doi.org/10.1111/jace.15749
43. Calisir I., D. Hall A., Chemical heterogeneity and approaches to its control in BiFeO3-BaTiO3 lead-free ferroelectrics, J. Mater. Chem. C, 2018, 6, 134–146.
44. Calisir I., Amirov A. A., Klepped A. K., Hall D. A., Optimisation of functional properties in lead-free BiFeO3-BaTiO3 ceramics through La3+ substitution strategy, J. Mater. Chem. A, 2018, 6, 5378-5397.
45. Lin D., Zheng Q., Li Y., Wan Y., Li Q., Zhou W., Microstructure, ferroelectric and piezoelectric properties of Bi0.5K0.5TiO3-modified BiFeO3–BaTiO3 lead-free ceramics with high Curie temperature, J. Eur. Ceram. Soc., 2013, 33, 3023–3036.
46. Yabuta H., Shimada M., Watanabe T., Hayashi J., Kubota M, Miura K, Fukui T, Fujii I, Wada S., Microstructure of BaTiO3-Bi(Mg1/2Ti1/2)O3-BiFeO3 Piezoelectric Ceramics, Jpn. J. Appl. Phys., 2012, 51, 09LD04.
47. Guo Y., Wang T., Shi D., Xiao P., Zheng Q., Xu C., Lam K. H., Lin D., Strong piezoelectricity and multiferroicity in BiFeO3–BaTiO3–NdCoO3 lead-free piezoelectric ceramics with high Curie temperature for current sensing application, J. Mater. Sci.: Mater. Electron., 2017, 28, 5531–5547.
48. Wang D., Cao M., Zhang S., Investigation of ternary system PbHfO3-PbTiO3-Pb(Mg1/3Nb2/3)O3 with morphotropic phase boundary compositions, J. Am. Ceram. Soc., 2012, 95, 3220–3228.
49. Guo Y., Xiao P., Wen R., Wan Y., Zheng Q., Shi D., Lam K. H., Liu M., Lin D., Critical roles of Mn-ions in enhancing the insulation, piezoelectricity and multiferroicity of BiFeO3, J. Mater. Chem. C, 2015, 3, 5811-5824.
50. Liu N., Liang R., Liu Z., Zhou Z., Xu C., Wang G., Dong X., Large remanent polarization and enhanced magnetic properties in non-quenched Bi(Fe,Ga)O3-(Ba,Ca)(Zr,Ti)O3 multiferroic ceramics, Appl. Phys. Lett., 2017, 110, 112902.

51. Zhang L., Jiang S., Fan B., Zhang G., Enhanced energy storage performance in (Pb0.858Ba0.1La0.02Y0.008)(Zr0.65Sn0.3Ti0.05)O3(Pb0.97La0.02)(Zr0.9Sn0.05Ti0.05)O3 anti-ferroelectric composite ceramics by Spark Plasma Sintering, J. Alloys Compd., 2015, 622, 162-165.
52. Liu Z., Chen X., Peng W., Xu C., Dong X., Cao F., Wang G., Temperature-dependent stability of energy storage properties of Pb0.97La0.02(Zr0.58Sn0.335Ti0.085)O3 antiferroelectric ceramics for pulse power capacitors, Appl. Phys. Lett., 2015, 106, 262901.
53. Zhang Q., Tong H., Chen J., Lu Y., Yang T., Yao X., He Y., High recoverable energy density over a wide temperature range in Sr modified (Pb,La)(Zr,Sn,Ti)O3 antiferroelectric ceramics with an orthorhombic phase, Appl. Phys. Lett., 2016, 109, 262901.
54. Xu R., Li B., Tian J., Xu Z., Feng Y., Wei X., Huang D., Yang L., Pb0.94La0.04[(Zr0.70Sn0.30)0.90Ti0.10]O3 antiferroelectric bulk ceramics for pulsed capacitors with high energy and power density, Appl. Phys. Lett., 2017, 110, 142904.
55. Zhang Q., Chen J., Lu Y., Yang T., Yao X., He Y., (Pb,Sm)(Zr,Sn,Ti)O3 Multifunctional Ceramics with Large Electric-Field Induced Strain and High-Energy Storage Density, J. Am. Ceram. Soc., 2016, 99, 3853-3856.
56. Zhao Q., Lei H., He G., Di J., Wang D., Tan P., Jin H., Cao M., Effects of thickness on energy storage of (Pb, La)(Zr, Sn, Ti)O3 antiferroelectric films deposited on LaNiO3 electrodes, Ceram. Int., 2016, 42, 1314-1317.
57. Yang H., Yan F., Lin Y., Wang T., Novel Strontium Titanate-Based Lead-Free Ceramics for High-Energy Storage Applications, ACS Sustainable Chem. Eng., 2017, 5,10215-10222.
58. Yan F., Yang H., Lin Y., Wang T., Dielectric and Ferroelectric Properties of SrTiO3-Bi0.5Na0.5TiO3-BaAl0.5Nb0.5O3 Lead-Free Ceramics for High-Energy-Storage Applications, Inorg. Chem., 2017, 56, 13510-13516.
59. Yin J., Lv X., Wu J., Enhanced energy storage properties of {Bi0.5[(Na0.8K0.2)1-zLiz]0.5}0.96Sr0.04 (Ti1-x-yTaxNby)O3 lead-free ceramics, Ceram. Inter., 2017, 43, 13541-13546.

60. Pu Y., Yao M., Zhang L., Chen M., Enhanced energy storage density of 0.55Bi0.5Na0.5TiO3-0.45Ba0.85Ca0.15Ti0.85Zr0.1Sn0.05O3 with MgO addition, J. Alloys Compd., 2017, 702, 171-177.

61. Tao H., Wu W., Wu J., Electrical properties of holmium doped (K,Na)(Nb,Sb)O3-(Bi,Na)HfO3 ceramics with wide sintering and poling temperature range, J. Alloys Compd., 2016, 689, 759-766.

62. Qu B., Du H., Yang Z., Liu Q., Liu T., Enhanced dielectric breakdown strength and energy storage density in lead-free relaxor ferroelectric ceramics prepared using transition liquid phase sintering, RSC Adv., 2016, 6, 34381–34389.

63. Tao H., Wu J., Optimization of energy storage density in relaxor (K, Na, Bi)NbO3 ceramics, J. Mater. Sci.: Mater. Electron., 2017, 28:16199–16204.

64. Saito Y., Takao H., Tani T., Nonoyama T., Takatori K., Homma T., Nagaya T., Nakamura M., Lead-free Piezoceramics, Nature, 2004, 432, 84−87.

65. Zhang S., Kounga A. B., Aulbach E., Ehrenberg H., Rödel J., Giant strain in lead-free piezoceramics Bi0.5Na0.5TiO3–BaTiO3–K0.5Na0.5NbO3 system, Appl. Phys. Lett., 2007, 91, 112906.

66. Wang D., Cao M., Zhang S., Investigation of ternary system Pb(Sn,Ti)O3–Pb(Mg1/3Nb2/3)O3 with morphotropic phase boundary compositions, J. Eur. Ceram. Soc., 2012, 32, 441–448.

67. Wang D., Li J., Cao M., Zhang S., Effects of Nb2O5 additive on the piezoelectric and dielectric properties of PHT-PMN ternary ceramics near the morphotropic phase boundary, Phys. Status Solidi A, 2014, 211, 226–230.

68. Qi H., Zuo R., Zheng D., Xie A., Evolution of relaxor behavior and high-field strain responses in Bi(Mg1/2Ti1/2)O3-PbTiO3-Pb(Ni1/3Nb2/3)O3 ferroelectric ceramics, J. Alloys Compd., 2017, 724, 774–781.

69. Donnelly N. J., Shrout T. R., Randall C. A., Addition of a Sr, K, Nb (SKN) Combination to PZT(53/47) for High Strain Applications, J. Am. Ceram. Soc., 2007, 90, 490–495.

70. Zhang Q., Chen J., Lu Y., Yang T., Yao X., He Y., (Pb,Sm)(Zr,Sn,Ti)O3 Multifunctional Ceramics with Large Electric-Field Induced Strain and High-Energy Storage Density, J. Am. Ceram. Soc., 2016, 99, 3853–3856.

71. Liu Z., Zhao C., Li J., Wang K., Wu J., Large strain and temperature-insensitive piezoelectric effect in high-temperature piezoelectric ceramics, J. Mater. Chem. C, 2018, 6, 456-463

72. Tao H., Wu J., Xiao D., Zhu J., Wang X., Lou X., ACS Appl. Mater. Interfaces, 2014, 6, 20358−20364.

73. Zheng T., Wu J., Xiao D., Zhu J., High Strain in (K,Na)NbO3-Based Lead-Free Piezoceramics, ACS Appl. Mater. Interfaces, 2015, 7, 20332−20341

74. Qin Y., Zhang J., Yao W., Lu C., Zhang S., Domain Configuration and Thermal Stability of (K0.48Na0.52)(Nb0.96Sb0.04)O3-Bi0.50(Na0.82K0.18)0.50ZrO3 Piezoceramics with High d33 Coefficient, ACS Appl. Mater. Interfaces, 2016, 8, 7257−7265.

75. Wang K., Yao F., Jo W., Gobeljic D., Shvartsman V. V., Lupascu D. C., Li J., Rödel J., Temperature-Insensitive (K,Na)NbO3-Based Lead-Free Piezoactuator Ceramics, Adv. Funct. Mater., 2013, 23, 4079–4086.

76. Fu J., Zuo R., Qi H., Zhang C., Li J., Li L., Low electric-field driven ultrahigh electrostrains in Sb-substituted (Na,K)NbO3 lead-free ferroelectric ceramics, Appl. Phys. Lett., 2014, 105, 242903.

77. Lee J., Kim D., Seo I., Kim J., Park J., Ryu J., Han S. H., Jang B., Nahm S., Large Strain in CuO-added (Na0.2K0.8)NbO3 Ceramic for Use in Piezoelectric Multilayer Actuators, J. Am. Ceram. Soc., 2016, 99, 938–945.

78. Zhang M., Wang K., Du Y., Dai G., Sun W., Li G., Hu D., Thong H. C., Zhao C., Xi X., Yue Z., Li J., High and Temperature-Insensitive Piezoelectric Strain in Alkali Niobate Lead-free Perovskite, J. Am. Chem. Soc. 2017, 139, 3889−3895

79. Wang X., Zheng T., Wu J., Xiao D., Zhu J., Wang H., Wang X., Lou X., Gu Y., Characteristics of giant piezoelectricity around the rhombohedral-tetragonal phase boundary in (K,Na)NbO3-based ceramics with different additives, J. Mater. Chem. A, 2015, 3, 15951-15961.

80. Zhou J., Wang K., Yao F., Zheng T., Wu J., Xiao D., Zhu J., Li J., Multi-scale thermal stability of niobate-based lead-free piezoceramics with large piezoelectricity, J. Mater. Chem. C, 2015, 3, 8780-8787.

81. Wang D., Hussain F., Khesro A. , Feteira A., Tian Y., Zhao Q., Reaney I. M., Composition and temperature dependence of structure and piezoelectricity in (1-x)(K1-yNay)NbO3-x(Bi1/2Na1/2)ZrO3 lead-free ceramics, J. Am. Ceram. Soc., 2017, 100, 627–637

82. Zhang S., Kounga A. B., Aulbach E., Granzow T., Jo W., Kleebe H. J., Rödel J., Lead-Free Piezoceramics with Giant Strain in the System Bi0.5Na0.5TiO3–BaTiO3–K0.5Na0.5NbO3. I. Structure and Room Temperature Properties, J. Appl. Phys., 2008, 103, 034107.

83. Wang Y., Kounga Njiwa A. B., Hoffmann C., WO/2011/012682, 2011

84. Bai W., Li P., Li L., Zhang J., Shen B., Zhai J., Structure evolution and large strain response in BNT–BT lead-free piezoceramics modified with Bi(Ni0.5Ti0.5)O3, J. Alloys Compd., 2015, 649, 772-781.

85. Maqbool A., Hussain A., Rahman J. U., Song T. K., Kim W., Lee J., Kim M., Enhanced electric field-induced strain and ferroelectric behavior of (Bi0.5Na0.5)TiO3–BaTiO3–SrZrO3 lead-free ceramics, Ceram. Inter, 2014, 40, 11905-11914.

86. Yoshii K., Hiruma Y., Nagata H., Takenaka T., Electrical Properties and Depolarization Temperature of (Bi1/2Na1/2)TiO3–(Bi1/2K1/2)TiO3 Lead-Free Piezoelectric Ceramics, Jpn. J. Appl. Phys., 2006, 45, 4493–6.

87. Pham K., Hussain A., Ahn C. W., Kim W., Jeong S. J., Lee J., Giant strain in Nb-doped Bi0.5(Na0.82K0.18)0.5TiO3 lead-free electromechanical ceramics, Mater. Lett., 2010, 64, 2219-2222.

88. Nguyen V., Han H., Kim K., Dang D., Ahn K., Lee J., Strain enhancement in Bi1/2(Na0.82K0.18)1/2TiO3 lead-free electromechanical ceramics by co-doping with Li and Ta, J. Alloys Compd., 2012, 511, 237–241.

89. Hiruma Y., Nagata H., Takenaka T., Formation of Morphotropic Phase Boundary and Electrical Properties of (Bi1/2Na1/2)TiO3-Ba(Al1/2Nb1/2)O-3 Solid Solution Ceramics, Jpn. J. Appl. Phys., 2009, 48, 09KC08.

90. Yang H., Yan F., Lin Y., Wang T., Enhanced recoverable energy storage density and high efficiency of SrTiO3-based lead-free ceramics, Appl. Phys. Lett., 2017, 111, 253903.

91. Yang H., Yan F., Lin Y., Wang T., He L., Wang F., A lead free relaxation and high energy storage efficiency ceramics for energy storage applications, J. Alloys Compd., 2017, 710, 436–445.

92. Yang H., Yan F., Lin Y., Wang T., Wang F., Wang Y., Guo L, Tai W., Wei H., Lead-free BaTiO3-Bi0.5Na0.5TiO3-Na0.73Bi0.09NbO3 relaxor ferroelectric ceramics for high energy storage, J. Eur. Ceram. Soc., 2017, 37, 3303–3311.

Figure Captions:

Fig. 1. a) Room temperature XRD patterns of BF-BT-xBZN from 20°~70° 2θ. b) Rietveld refinement analysis of BF-BT-0.05BZN using the GSAS+EXPGUI package. c) Temperature dependence of ε_r and tanδ for BF-BT-xBZN; (d) Spectroscopic plots of Z'' and M'' for BF-BT-0.05BZN.

Fig. 2. SEM images of polished surfaces for BF-BT-xBZN (a) BF-BT, (b) BF-BT-0.02BZN and (c) BF-BT-0.05BZN. EDS elemental mapping results of polished BF-BT-0.05BZN samples (d) Ba, (e) Ti, (f) Bi, (g) Fe, (h) O, (i) Zn, (j) Nb and (k) elemental layered image.

Fig. 3. a) Bright field TEM image of a grain in BF-BT-0.05BZN, illustrating a $BiFeO_3$ rich core and $BaTiO_3$ rich shell; <211> zone axis diffraction patterns reveal the absence of ½{ooo} superstructure reflections in the shell (up) compared with core regions (down). b) The $BiFeO_3$ and $BaTiO_3$ core-shell regions are tentatively ascribed to the high and low temperature dielectric anomalies.

Fig. 4. High electric field (a) bipolar P-E, (b) bipolar S-E and (c) unipolar S-E loops of BF-BT-xBZN samples at 100 kV/cm. (d) P_r and E_C as a function of BZN concentration. (e) S_{pos} and S_{neg} as a function of BZN concentration. (f) d_{33}^* and *SH* as a function of BZN concentration. d_{33} as a function of BZN concentration is in the inset of (d).

Fig. 5. Unipolar P-E loops under different electric fields for (a) BF-BT-0.05BZN and (b) BF-BT-0.08BZN. W, W_{rec} and η as a function of electric field for (c) BF-BT-0.05BZN and (d) BF-BT-0.08BZN.

Fig. 6. Time dependence of the pulsed discharge current for (a) BF-BT-0.05BZN and (b) BF-BT-0.08BZN. Time dependence of W_{rec} for (c) BF-BT-0.05BZN and (d) BF-BT-0.08BZN.

Fig. 7. *In-situ* temperature dependence of (a) J and (b) unipolar P-E loops for BF-BT-0.05BZN at an electric field of 120 kV/cm. (c) J as a function of temperature at different electric fields. (d) W, W_{rec} and η as a function of temperature.

Fig. 8. Comparison of (a) W_{rec} vs electric field and (b) strain vs d_{33}^* among lead-based and lead-free ceramics.[12-25, 26-36, 48-92]

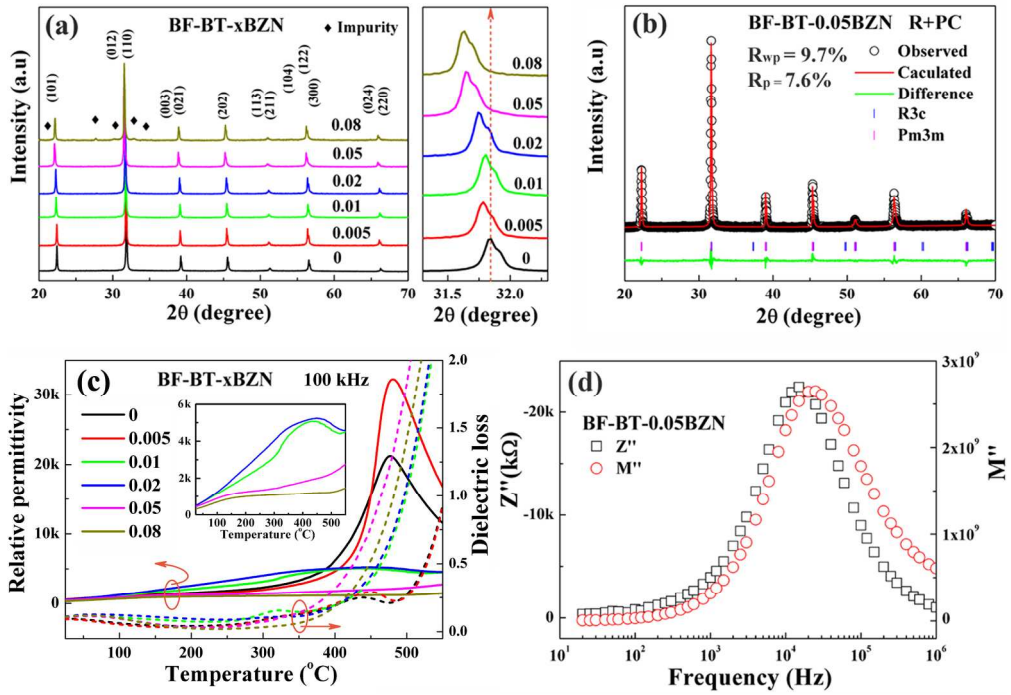

Fig. 1. a) Room temperature XRD patterns of BF-BT-xBZN from 20°~70° 2θ. b) Rietveld refinement analysis of BF-BT-0.05BZN using the GSAS+EXPGUI package. c) Temperature dependence of εr and tanδ for BF-BT-xBZN; (d) Spectroscopic plots of Z'' and M'' for BF-BT-0.05BZN.

182x127mm (300 x 300 DPI)

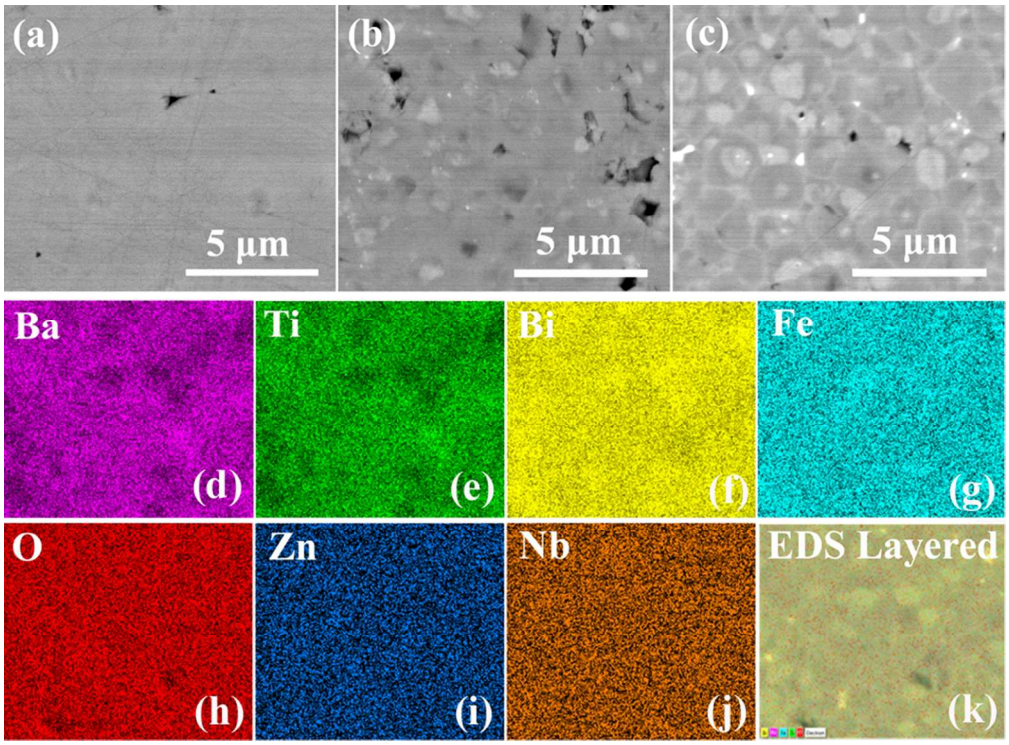

Fig. 2. SEM images of polished surfaces for BF-BT-xBZN (a) BF-BT, (b) BF-BT-0.02BZN and (c) BF-BT-0.05BZN. EDS elemental mapping results of polished BF-BT-0.05BZN samples (d) Ba, (e) Ti, (f) Bi, (g) Fe, (h) O, (i) Zn, (j) Nb and (k) elemental layered image.

84x62mm (300 x 300 DPI)

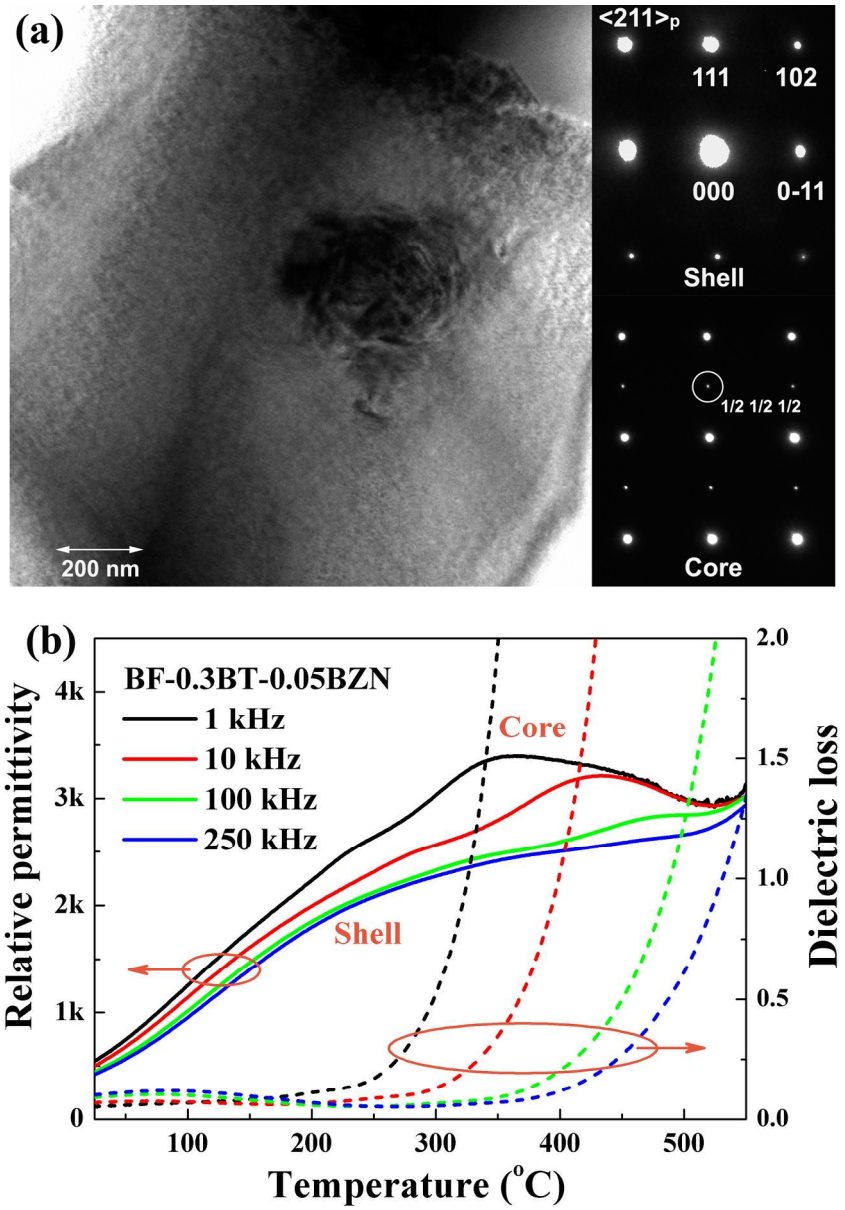

Fig. 3. a) Bright field TEM image of a grain in BF-BT-0.05BZN, illustrating a BiFeO3 rich core and BaTiO3 rich shell; <211> zone axis diffraction patterns reveal the absence of ½{ooo} superstructure reflections in the shell (up) compared with core regions (down). b) The BiFeO3 and BaTiO3 core-shell regions are tentatively ascribed to the high and low temperature dielectric anomalies.

169x242mm (300 x 300 DPI)

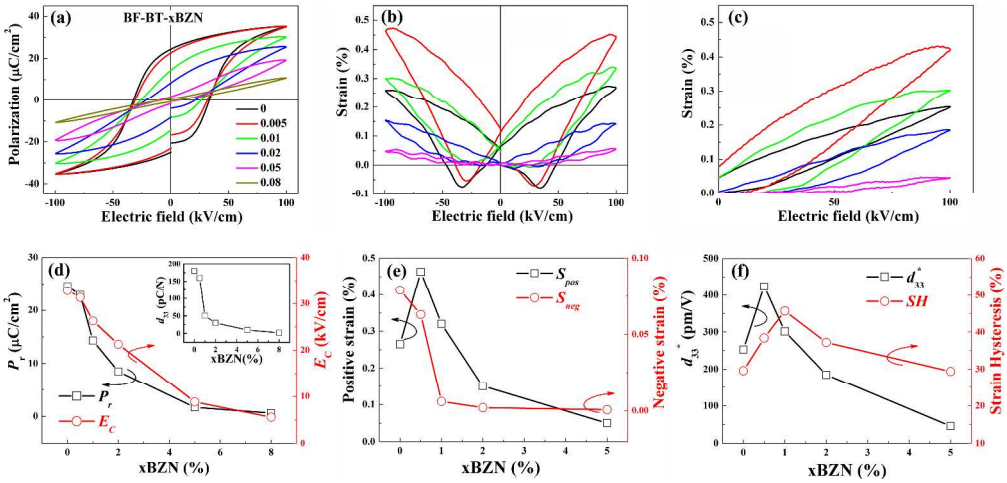

Fig. 4. High electric field (a) bipolar P-E, (b) bipolar S-E and (c) unipolar S-E loops of BF-BT-xBZN samples at 100 kV/cm. (d) Pr and EC as a function of BZN concentration. (e) Spos and Sneg as a function of BZN concentration. (f) d33* and SH as a function of BZN concentration. d33 as a function of BZN concentration is in the inset of (d).

777x369mm (300 x 300 DPI)

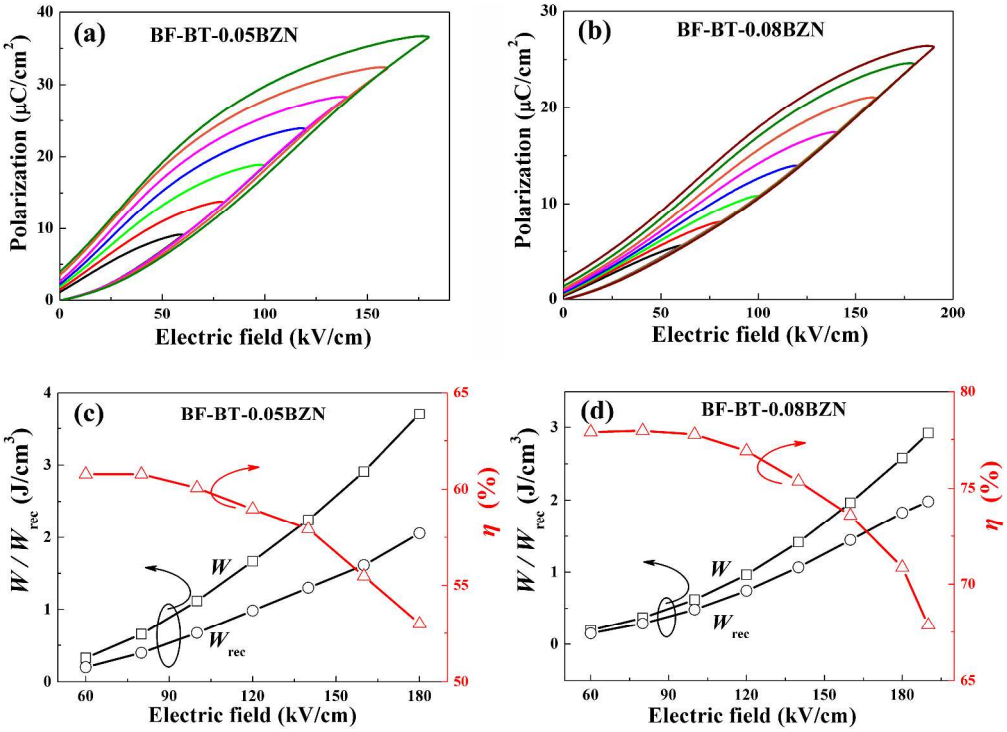

Fig. 5. Unipolar P-E loops under different electric fields for (a) BF-BT-0.05BZN and (b) BF-BT-0.08BZN. W, Wrec and η as a function of electric field for (c) BF-BT-0.05BZN and (d) BF-BT-0.08BZN.

508x368mm (300 x 300 DPI)

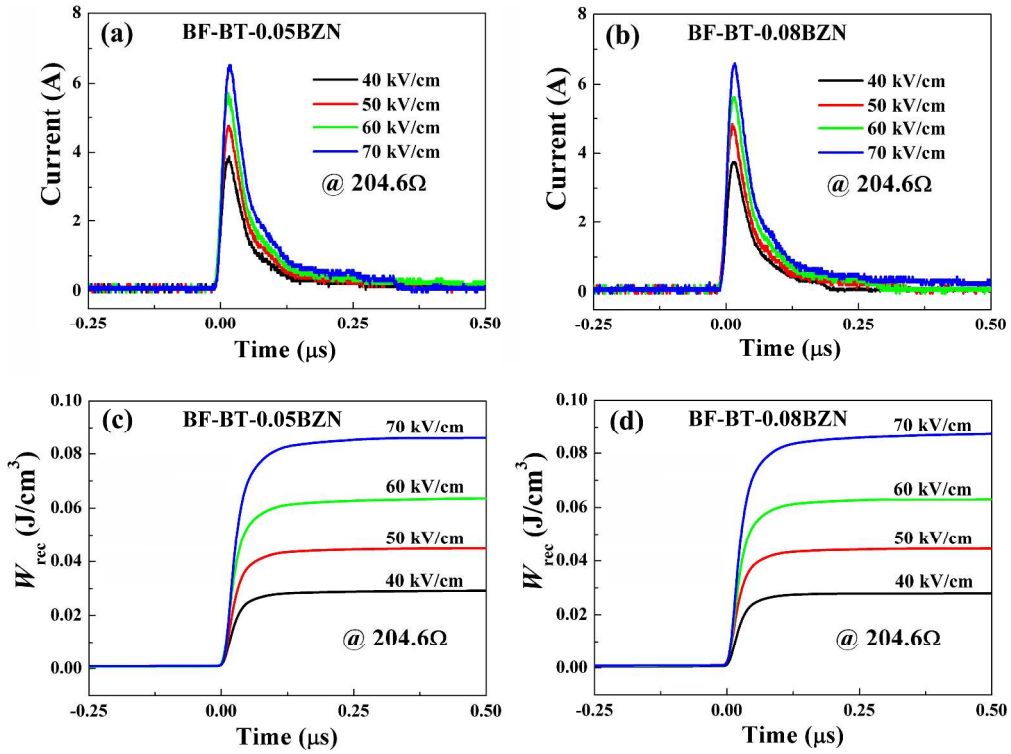

Fig. 6. Time dependence of the pulsed discharge current for (a) BF-BT-0.05BZN and (b) BF-BT-0.08BZN. Time dependence of Wrec for (c) BF-BT-0.05BZN and (d) BF-BT-0.08BZN.

497x370mm (300 x 300 DPI)

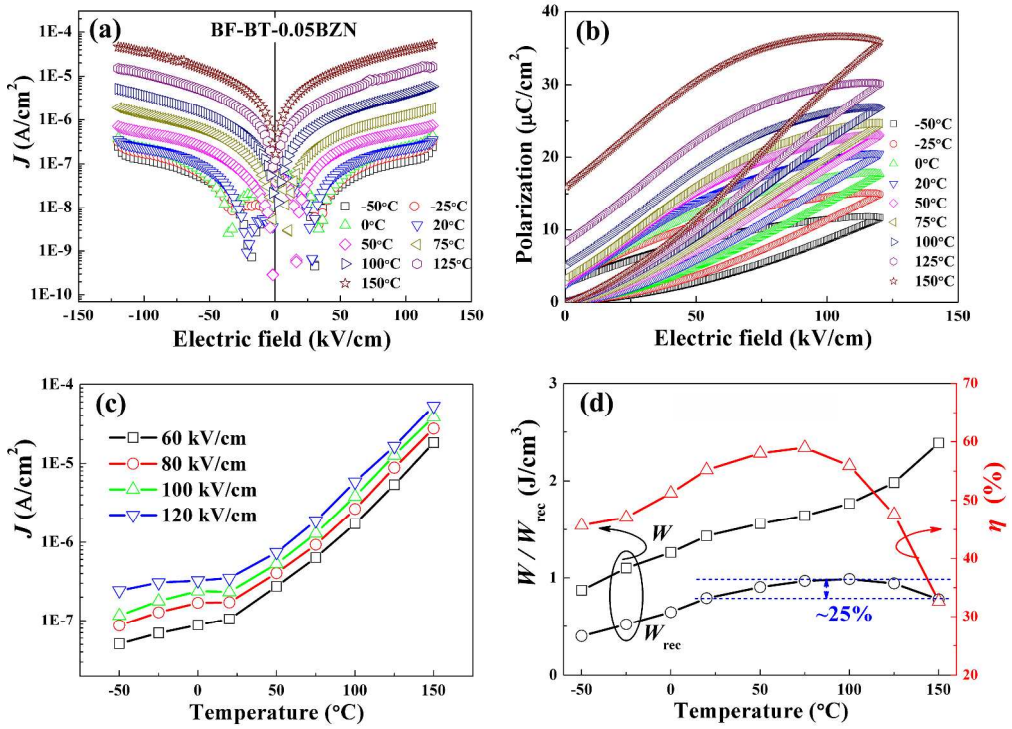

Fig. 7. In-situ temperature dependence of (a) J and (b) unipolar P-E loops for BF-BT-0.05BZN at an electric field of 120 kV/cm. (c) J as a function of temperature at different electric fields. (d) W, Wrec and η as a function of temperature.

503x364mm (300 x 300 DPI)

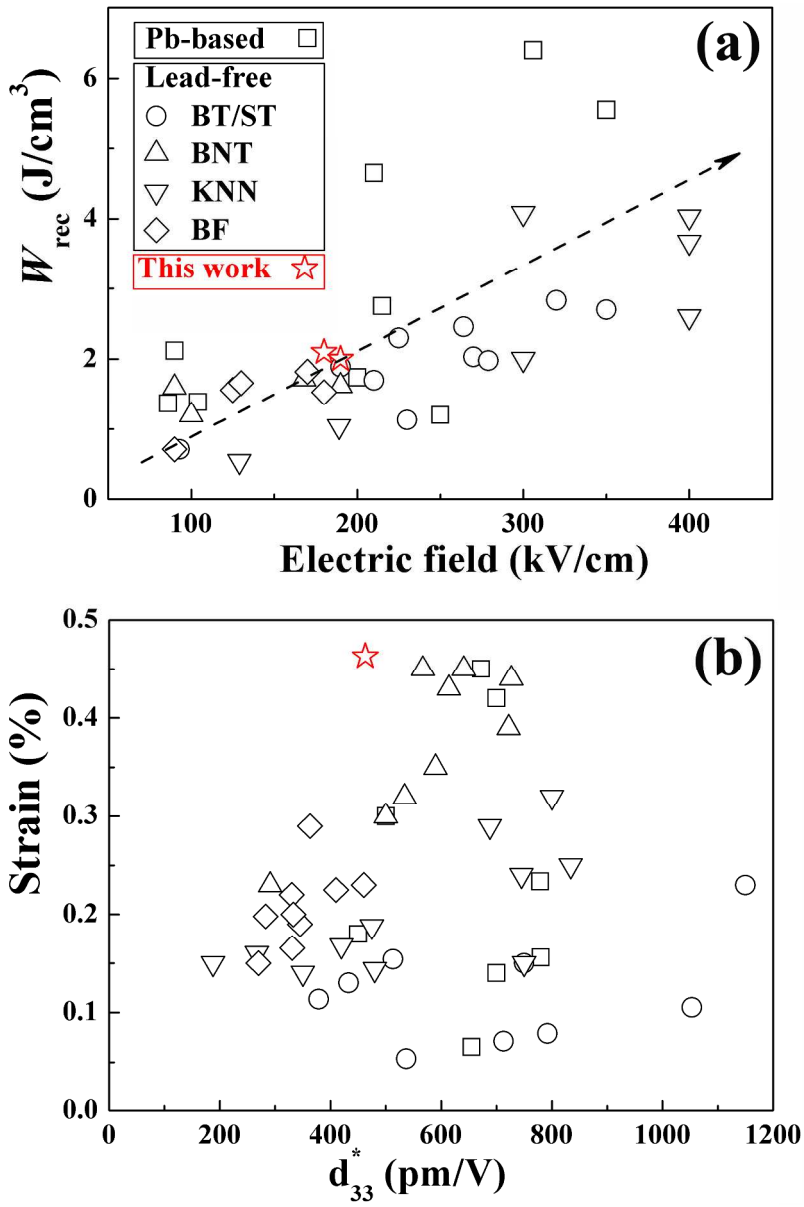

Fig. 8. Comparison of (a) Wrec vs electric field and (b) strain vs d33* among lead-based and lead-free ceramics.12-25, 26-36, 45-86

423x636mm (300 x 300 DPI)

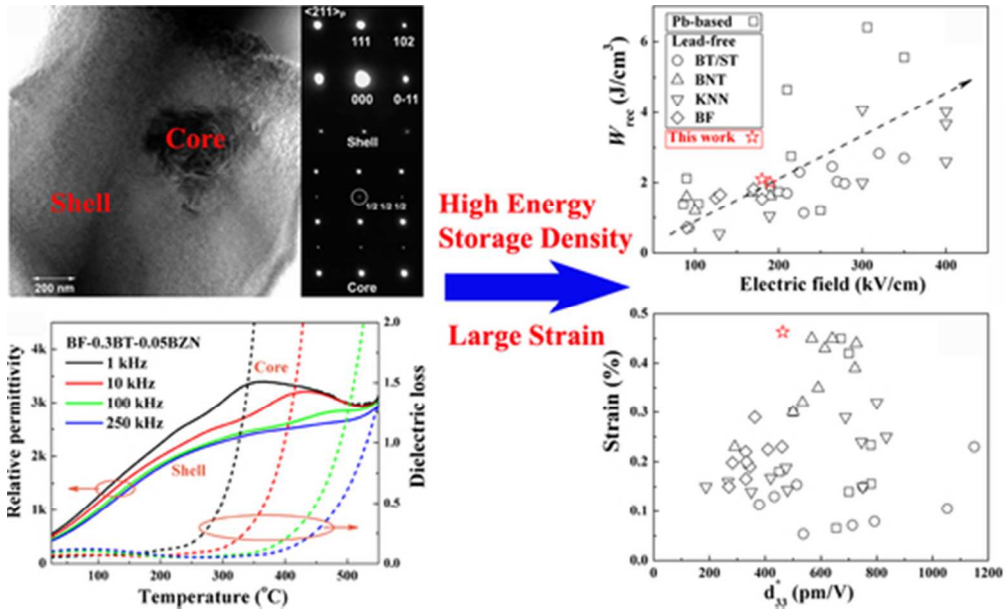

For Table of Contents Only

44x26mm (300 x 300 DPI)